Study of Shear Thinning in High Polymer Solution Using Dynamic NMR Microscopy

Y. Xia and P. T. Callaghan*

Department of Physics and Biophysics, Massey University, Palmerston North, New Zealand

Received November 27, 1990; Revised Manuscript Received February 26, 1991

ABSTRACT: Dynamic NMR imaging has been used to measure velocity profiles for water solutions of WSR301 poly(ethylene oxide) in laminar flow through a 700-μm-i.d. capillary as a function of concentration and pressure gradient. A transition from Poiseuille flow to power law shear thinning is apparent as the concentration is increased above c^*. Equilibrium self-diffusion coefficients have been measured as a function of concentration for WSR301 and as a function of molar mass for monodisperse poly(ethylene oxide) standards in D_2O, and it is apparent that the data are consistent with the usual reptative scaling behavior. A measurement of self-diffusion in the presence of the flow field indicates that shear thinning is associated with significant enhancement of the polymer Brownian motion along the axis of shear, and these data are interpreted by using a simple adaptation of the entanglement/blob model.

Introduction

High polymer melts and solutions exhibit unusual rheological properties. Among the nonlinear viscoelastic properties of such complex liquids is the non-Newtonian dependence of the shear stress on shear rate,[1] commonly known as shear thinning. A number of constitutive equations have been developed to describe the relationship between the shear stress, σ_{xy}, upon the shear rate, $\dot{\gamma} = \partial v_x/\partial y$, in simple Couette flow shown in Figure 1, one of the better known being that of the "power law" fluid[2]

$$\sigma_{xy} = K\dot{\gamma}^n \tag{1}$$

where K and n are constants for a particular fluid. Hence, the nonlinear viscosity, η, may be written

$$\eta(\dot{\gamma}) = K\dot{\gamma}^{n-1} \tag{2}$$

The power law exponent, n, is unity for a Newtonian fluid and less than unity for a shear-thinning fluid. Clearly, the power law constitutive equation is phenomenological and suffers from a number of defects, including the divergence of the viscosity at zero shear in the case of shear-thinning behavior. Nonetheless, it does provide quite a good empirical description in a number of experiments.

One of the challenges of polymer physics is to find a molecular basis for the constitutive equations. In Doi–Edwards theory[3-6] the constitutive equation for entangled polymers is derived from the reptation model and the onset of shear thinning is associated with a shear rate comparable with the slowest polymer relaxation process, the rate of tube disengagement, τ_d^{-1}, where τ_d is the tube renewal time. $\eta(\dot{\gamma})$ is given by the product of the zero-shear viscosity, η_0, and the relaxation function $h(\dot{\gamma}\tau_d)$ shown in Figure 2. Clearly, since the viscosity decreases more rapidly than $\dot{\gamma}^{-1}$ for $\dot{\gamma}\tau_d \gg 1$, the shear stress must begin to decrease at some specific shear rate. This is the basis of the so-called "spurt effect" predicted for polymers in shear flow.[7,8] Measurement of the shear-dependent viscosity provides a classical macroscopic test of the model. By contrast, the microscopic tests of reptation theory usually involve a measurement of the molecular dynamics and, in particular, the Brownian motion. In this regard, center-of-mass self-diffusion (D_s) data under zero-shear conditions has provided a test[9] of scaling laws based on the entanglement tube reptation model.[3,6,10-12] For a semidilute solution ($c > c^*$) the relevant scaling laws for molar

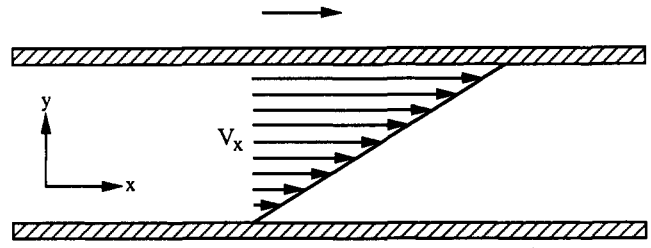

Figure 1. Couette flow for a Newtonian fluid in which the shear stress is directly proportional to the rate of strain.

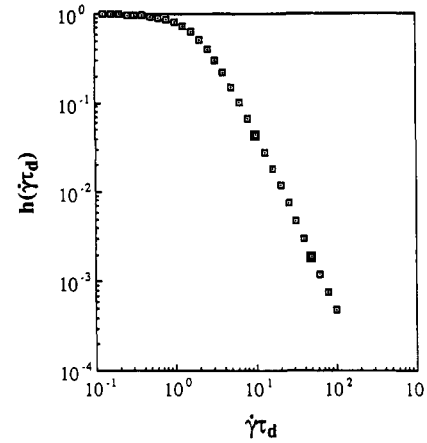

Figure 2. Doi–Edwards relaxation function $h(\dot{\gamma}\tau_d)$, which relates the shear-dependent viscosity to the shear rate $\dot{\gamma}$ for an entangled polymer with tube disengagement time τ_d. Note that $\eta = \eta_0 h(\dot{\gamma}\tau_d)$ where η_0 is the zero-shear viscosity.

mass M and polymer concentration are[6,13]

$$D_s \sim M^{-2}c^{(2-\nu)/(1-3\nu)} \tag{3a}$$

$$\tau_d \sim M^3 c^{(3\nu-3)/(1-3\nu)} \tag{3b}$$

$$\eta_0 \sim M^3 c^{3/(1-3\nu)} \tag{3c}$$

where ν is the index relating the random-coil end-to-end distance to the number of monomeric subunits (i.e., $R_0 \sim M^\nu$) and takes a value between 0.5 and 0.6 depending on the degree to which the polymer coil obeys Gaussian or excluded-volume statistics, an effect governed by solvent quality. It should be noted that the same molar mass

0024-9297/91/2224-4777$02.50/0

scaling laws apply for polymer melts provided that $M > M_c$ where M_c is the critical molar mass for the onset of entanglements.[1]

To date, measurements of self-diffusion have been carried out only under zero-shear conditions. It would be interesting to monitor the Brownian motion under shear, and especially under shear rates sufficiently high to induce shear-thinning effects. If shear thinning does arise from a breakdown in entanglement renewal as adjacent polymers separate, then the perturbation to the tube should cause a dramatic enhancement in D_s, as measured in the local frame of reference. Such measurements are made possible by the development of a new technique known as dynamic NMR microscopy,[14,15] which offers a number of advantages over high-resolution laser Doppler velocimetry. In particular, NMR measurement is not restricted to transparent liquids and requires no particulate dopant to enhance scattering. Furthermore, dynamic NMR microscopy is sensitive to molecular length scales and can detect Brownian motion in the local frame of reference. Using this method, we have measured velocity and self-diffusion profiles for high molar mass poly(ethylene oxide) molecules in solution undergoing laminar flow through a 700-μm-i.d. capillary. The inherent spatial resolution of the tomographic method employed has enabled us to measure D_s values as a function of local shear rate right across the capillary. The aim of this work is to elucidate the molecular origins of rheological behavior in this system.

Dynamic NMR Microscopy

Nuclear magnetic resonance imaging utilizes magnetic field gradients to impart a spatial signature to the nuclear spin precession. Consequently the local nuclear Larmor frequency may be written as $\omega(\mathbf{r}) = \gamma \mathbf{G}\cdot\mathbf{r}$ where $\mathbf{G}$ is the gradient, γ the nuclear gyromagnetic ratio, and $\mathbf{r}$ the nuclear spatial coordinates. The evolution of the free precession may be written ideally as[16]

$$S(\mathbf{k}) = \int \rho(\mathbf{r}) \exp[i(2\pi \mathbf{k}\cdot\mathbf{r})]\, d\mathbf{r} \qquad (4)$$

where $\rho(\mathbf{r})$ is the nuclear spin density and $\mathbf{k}$ is the reciprocal space dimension conjugate to $\mathbf{r}$ and is given by $(1/2\pi)\gamma \mathbf{G}t$, t being the evolution time. The nuclear spin density can be reconstructed by acquiring $S(\mathbf{k})$ over some appropriate volume of $\mathbf{k}$ space and performing an inverse Fourier transformation. Generally, reconstruction is carried out in two dimensions by using a plane of spins prepared by a frequency-selective excitation. This latter process is known as slice selection and is a standard procedure in NMR imaging. Given suitably optimized receiver and gradient coil configurations, it is possible to reconstruct an image from hydrogen nuclei (the most sensitive spins) with a voxel resolution below $(100\ \mu m)^3$. Such imaging is known as NMR microscopy.

Equation 4 has a formal similarity with the relation that governs the echo amplitude and phase in a pulsed gradient spin echo (PGSE) experiment.[17,18] Here the phase shifts acquired do not arise from the spin positions but from their motions over a well-defined time scale, Δ, the time separating the gradient pulses of duration δ and amplitude g. In the narrow gradient pulse approximation the echo amplitude is given by

$$E_\Delta(\mathbf{q}) = \int \bar{P}_s(\mathbf{R},\Delta) \exp[i(2\pi \mathbf{q}\cdot\mathbf{R})]\, d\mathbf{R} \qquad (5)$$

where $\bar{P}_s(\mathbf{R},\Delta)$ is the average propagator corresponding to the probability that any spin will move by a distance $\mathbf{R}$ over the time Δ. $\mathbf{q}$ is conjugate to $\mathbf{R}$ and is given by $(1/2\pi)\gamma \mathbf{g}\delta$. For simple Brownian motion, $\bar{P}_s(\mathbf{R},\Delta)$ is a Gaussian function, $(4\pi D_s\Delta)^{-3/2} \exp(-\mathbf{R}^2/4D_s\Delta)$, and eq 5 leads to the well-known Stejskal–Tanner relation[17]

$$E_\Delta = \exp(-\gamma^2 g^2 \delta^2 D_s \Delta) \qquad (6)$$

where for finite gradient pulse durations Δ is replaced by $(\Delta - \delta/3)$. The PGSE experiment has been widely used to measure self-diffusion in polymer melts and solutions.[19-23]

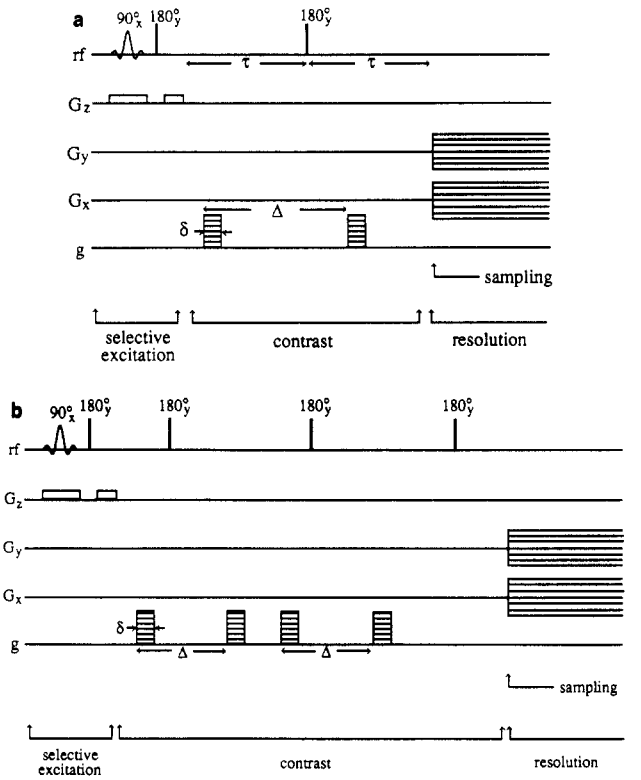

Figure 3. Pulse sequences for dynamic NMR imaging in which G_x, G_y, and G_z refer to the tomography gradients while g refers to the PGSE gradient used to phase encode for motion: (a) Single PGSE phase-encoding in which velocity and diffusion cause a contrast in the image. (b) Double PGSE phase-encoding in which phase shifts due to velocity are cancelled and only the stochastic motion introduces contrast.

By analogy with eq 4, it is clear that the eq 5 can be regarded as a form of imaging in which inverse Fourier transformation with respect to $\mathbf{q}$ enables $\bar{P}_s(\mathbf{R},\Delta)$ to be reconstructed. This approach offers specific advantages when the motion is complicated. For example, when the Brownian motion is superposed on an underlying velocity $\mathbf{v}$, the echo attenuation is phase modulated by a term $\exp[i(2\pi \mathbf{q}\cdot\mathbf{v}\Delta)]$ and Fourier reconstruction leads to a Gaussian function appropriately shifted along the displacement axis. Generally, we shall be concerned with one-dimensional displacements, Z, along the applied gradient direction so that reconstruction leads to the convolution

$$\bar{P}_s(Z,\Delta) = (4\pi D_s\Delta)^{-1/2} \exp(-Z^2/4D_s\Delta) \otimes \delta(Z - v\Delta) \qquad (7)$$

In dynamic NMR microscopy the $\mathbf{k}$- and $\mathbf{q}$-space imaging methods are combined as shown in the pulse sequence of Figure 3a. Now $E_\Delta(q)$ is a contrast in the image so that

$$S(\mathbf{k},\mathbf{q}) = \int \rho(\mathbf{r}) E_\Delta(\mathbf{q}) \exp[i(2\pi \mathbf{k}\cdot\mathbf{r})]\, d\mathbf{r} \qquad (8)$$

Double inverse Fourier transformation with respect to $\mathbf{k}$ and $\mathbf{q}$ returns $\bar{P}_s(Z,\Delta)$ for every pixel in the image. In this manner maps of D_s and $\mathbf{v}$ may be constructed. The method is described in detail elsewhere.[15,24]

In the specific application to be discussed here, velocity and diffusion maps are obtained for high polymer solution

Table I
Poly(ethylene oxide) Samples

	M_w	M_w/M_n
PEO standards	23 000	1.08
	56 300	1.05
	105 000	1.06
	253 000	1.07
	400 000	1.08
	750 000	1.13
	847 000	1.16
WSR301	$\sim 3 \times 10^6$	~1.6

in laminar flow through a narrow capillary tube. In the case of both the self-diffusion and velocity, the direction of motion measured is parallel to the capillary axis, although, in principle, it is possible to make measurements in any direction. A feature of the experiment is the existence of a velocity shear, which varies from zero at the center of the flow to a maximum at the edges. Because of the finite transverse resolution employed (around 15 μm), there will be a velocity gradient within the imaging pixels, which naturally leads to phase-spreading effects in a manner akin to self-diffusion. It is therefore essential to distinguish such a spread from that which arises from the Brownian motion if accurate self-diffusion maps are to be obtained. The method used relies on the fact that the local molecular velocities are constant over the evolution time of the spin echo. In consequence, use of a double PGSE sequence, shown in Figure 3b, causes the coherent phase shifts due to velocity spreading to be refocused while the spreading due to the underlying stochastic motion persists.[15] Of course, diffusion transverse to the flow will upset this assumption, but it is easy to show that such an effect will lead to insignificant perturbations to the apparent longitudinal diffusion coefficient provided that the shear rate is less than Δ^{-1}. The requirement restricts us to $\dot{\gamma} \leq 100\ s^{-1}$ in the measurement of diffusion maps. We shall therefore wish to use polymer systems whose tube renewal times are longer than a few milliseconds if shear-thinning effects are to be examined via the self-diffusion coefficients. Note that this requirement means that we will be measuring self-diffusion over a time scale, Δ, smaller than τ_d. At first sight it may appear that the observed motion will be dominated by internal modes of the polymer chain rather than the desired center of mass motion. In fact, significant internal motion is only observed provided that the applied magnetic field gradient is sufficiently large that $2\pi q$ considerably exceeds the inverse polymer dimensions, R_0^{-1}. For measurements using low q, center of mass motion will strongly influence the spin-echo decay even for $\Delta < \tau_d$. However, where both $\Delta < \tau_d$ and $2\pi q < R_0^{-1}$, the echo attenuation will be weak and D_s difficult to measure.

Experimental Section

Monodisperse poly(ethylene oxide) (PEO) samples were obtained from Polymer Laboratories (Church Stretton, Shropshire, England), while polydisperse high molar mass poly(ethylene oxide), WSR301, was obtained from Union Carbide (New York). Table I summarizes the properties of these polymers. A modified JEOL FX60 NMR spectrometer was used both for the dynamic NMR microscopy experiments and for equilibrium diffusion measurements on PEO/water samples. Equilibrium self-diffusion measurements were made for stationary samples of PEO dissolved in deuterium oxide by using 4-mm-diameter sealed NMR tubes. These experiments were performed by using a high-gradient PGSE probe developed in our laboratory, which could provide gradient amplitudes up to 17.7 T m^{-1}. Pulse durations (δ) and separation times (Δ) were in the range 4.5–65 ms and 20–200 ms. Self-diffusion coefficients so obtained were time-scale independent and reflect the center-of-mass Brownian motion. The dynamic NMR microscopy experiments were carried out by using a specially constructed imaging probe incorporating G_x, G_y, and G_z gradient coils, the y direction being aligned with the capillary axis. The G_x and G_z coils were used to map the spins in **k** space, and the G_y coil was used for slice selection and to provide the PGSE gradient pulses. This G_y coil was capable of generating gradients up to 7.31 T m^{-1}. All equilibrium self-diffusion and dynamic NMR microscopy experiments were carried out at ambient temperature, which was close to 30 °C.

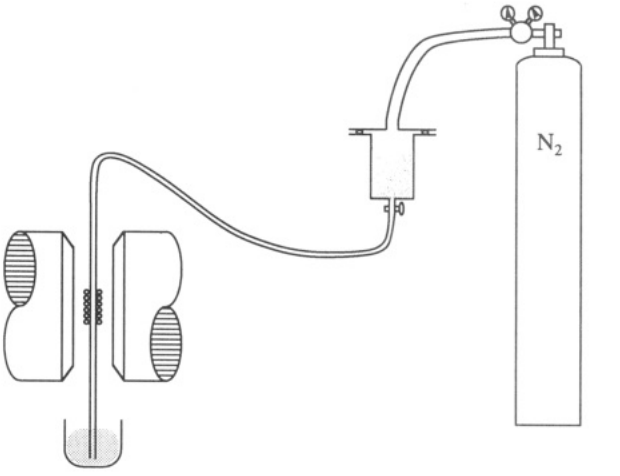

Figure 4. Schematic of the experimental arrangement for capillary flow imaging. The upper reservoir is pressurized by up to 21 atm in order to produce steady-state flow of a viscous polymer solution through the 700-μm-i.d. Teflon capillary.

Because WSR301 poly(ethylene oxide) is polydisperse, it is necessary to consider the averaging process appropriate to PGSE NMR diffusion measurements. It may be shown that where an effective diffusion coefficient, D_{eff}, is calculated from the initial slope of a Stejskal–Tanner plot, then D_{eff} is approximately related to the diffusion coefficient for the weight-averaged molar mass, $D(M_w)$, by[25,26]

$$D_{eff} = D(M_w) \exp\{(\sigma^2/2)\alpha(\alpha - 2)\} \quad (9)$$

where $M_w/M_n = \exp(\sigma^2)$ and α is the exponent that describes how D scales with M. The polydispersity of WSR301 was estimated by using a gel permeation chromatography column calibrated using the poly(ethylene oxide) standards shown in Table I. These measurements suggest $M_w/M_n = 1.6$ while the peak mass value is close to 1×10^6. The nominal $\bar{M}_w$ of WSR301 is 4×10^6. This discrepancy is characteristic of the method dependence associated with molar mass measurement for a polydisperse polymer.

The arrangement for the dynamic NMR microscopy experiment is shown schematically in Figure 4. A 120-cm^3 pressurized reservoir is connected to 0.7-mm-i.d. HPLC tubing made of Teflon, and a polymer solution is forced through the NMR imaging probe at a steady rate, which is controlled by adjusting the applied pressure between 0 and 21 atm. Because a large volume of polymer solution is required, these experiments were carried out by using the WSR301 PEO for which a large mass of material is available at low cost. Velocity and diffusion profiling experiments were carried out by using PEO/H_2O solutions with concentrations ranging from 0.5% to 4.5% w/v in which 0.1% $CuSO_4$ had been added in order to reduce the water proton T_1 relaxation time, therefore, enhancing the available signal-to-noise ratio. This doping appeared to have no influence on the polymer solubility or upon the equilibrium polymer self-diffusion coefficients. Because the proton NMR signal is dominated by the solvent hydrogen nuclei in these measurements, the molecular self-diffusion coefficients so obtained correspond to the water molecules. The velocity maps should, however, reflect the combined flow of the polymer and solvent in the solution. The slice thickness in these experiments was 2 mm while the transverse pixel resolution is 15 μm. Eighteen successive real and imaginary q-space slices were obtained over a total measurement time of approximately 3 h.

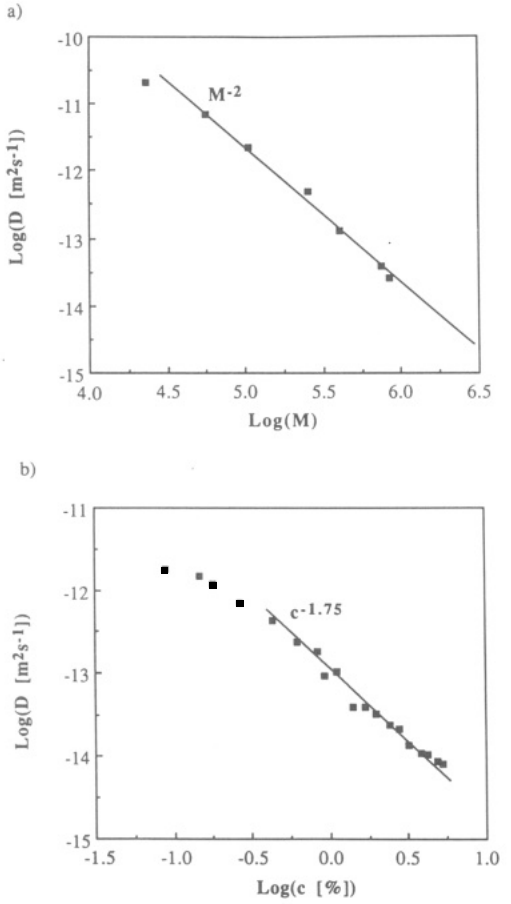

Figure 5. (a) Double-logarithmic plot of polymer self-diffusion versus molar mass for poly(ethylene oxide) standards at 5.0% w/v concentration in D_2O at 30 °C. (b) Double-logarithmic plot of polymer self-diffusion versus concentration (% w/v) for WSR301 poly(ethylene oxide) in D_2O at 30 °C.

In order to obtain polymer self-diffusion coefficients, the experiments were repeated by using PEO/D_2O solutions. For these experiments the much weaker proton NMR signal presented a special challenge in obtaining high spatial resolution. To circumvent this problem, we have taken advantage of the inherent azimuthal symmetry by reconstructing the diffusion-contrasted images from a single projection obtained from 4000 successive signal coadditions. This single-projection approach has been thoroughly tested in velocity mapping experiments and precisely reproduces the velocity maps obtained by using independently reoriented projection reconstruction. In 9 separate experiments, 10 different gradient real and imaginary q-slices were obtained and the diffusion coefficients for each pixel computed from the modulus images. The resulting diffusion maps for each experiment had poor signal-to-noise ratios so that the maps from the independent experiments were coadded. This addition process was checked by first coadding the individual modulus images corresponding to the same gradient slices and then recalculating the diffusion map.

At shear rates much higher than those employed in this work it is possible to break the polymer covalent bonds. As a test that the poly(ethylene oxide) molecules were undamaged in the present experiments we have repeated equilibrium self-diffusion measurements on a sample taken from the outflow reservoir and find polymer D_s values identical with those in fresh solutions.

Results

Figure 5a shows equilibrium self-diffusion data for different molar mass PEO molecules in D_2O at 5.0% w/v concentration. It is clear that above 50 000 the data are consistent with the usual $D_s \sim M^{-2}$ scaling characteristic of random-coil polymers with concentrations above c^*, the minimum concentration for the onset of entanglements.

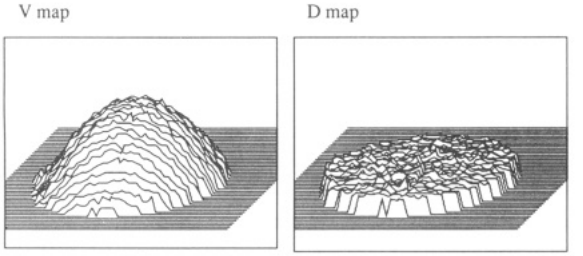

Figure 6. Velocity and self-diffusion maps for a 0.5% w/v poly(ethylene oxide)/water solution in flow through a 700-μm-i.d. capillary.

The concentration dependence of self-diffusion for WSR301 PEO in D_2O is shown in Figure 5b. Despite the polydispersity of this material, the apparent scaling behavior is remarkably close to $D_s \sim c^{-1.75}$, consistent with a random-coil exponent, $\nu = 0.6$. It is not our intention here to argue the issue of whether such behavior represents verification of the scaling hypotheses but merely to emphasize three points. First, it is clear that poly(ethylene oxide)/water exhibits self-diffusion behavior similar to that observed by using both forced Rayleigh scattering and PGSE NMR on a number of other polymer systems in the semidilute regime. Second, it is likely that the transition from dilute to semidilute behavior for WSR301 PEO in water is in the concentration range 0.5–1% w/v and that this polymer is clearly entangled at the concentration of 4.5% w/v used in the diffusion mapping experiment later described. Finally, by comparing the equilibrium self-diffusion data in parts a and b of Figure 5, we may estimate the PSGE NMR effective molar mass for WSR301 to be in the vicinity of 1.6×10^6. Use of eq 9 yields $M_w = 3.2 \times 10^6$, which is reasonably close to the nominal value quoted by the manufacturers.

Another estimation of the molar mass of WSR301 poly(ethylene oxide) may be obtained by estimating D_0, the self-diffusion coefficient in the zero concentration. Given the difficulty in obtaining a self-diffusion coefficient at very low concentrations, we find $D_0 \cong (2.5 \pm 0.5) \times 10^{-12}$ $m^2\ s^{-1}$. By comparison with the data of Bortel and Kochanowski,[27] the end-to-end length of the polymer, R_0, may be estimated as 1500 ± 300 Å.

Velocity and diffusion maps for WSR301 poly(ethylene oxide) in water at 0.5% concentration flowing under a 3.9-kPa pressure head are shown in Figure 6 while a corresponding velocity and diffusion profile through a diametral chord is given in Figure 7. The central maximum velocity, v_{max}, is 6.5 mm s^{-1} while the maximum shear rate, apparent at the edge of the flow, is approximately 40 s^{-1}. It is apparent that the velocity profile closely resembles the Poiseuille flow characteristic of a Newtonian fluid while the water self-diffusion is uniform across the flow field. These results are qualitatively similar to those obtained in independent experiments using pure water.

As the polymer concentration is increased above c^* a transition in the shear dependence of the viscosity is observed. The progression is illustrated in Figure 8 where normalized velocity profiles are shown for various concentrations between 0.5% and 4.5% w/v. Above 1% the Poiseuille behavior is clearly perturbed. For convenience we have attempted to fit the data using a power law constitutive equation for which the solution to the Navier–Stokes equation is given by[2]

$$v(r) = \left(\frac{\Delta P}{2K\Delta L}\right)^{1/n}\left(\frac{n}{n+1}\right)[R^{(n+1)/n} - r^{(n+1)/n}] \qquad (10)$$

where $\Delta P/\Delta L$ is the pressure gradient and R is the inside radius of the capillary. It should be noted that eq 10

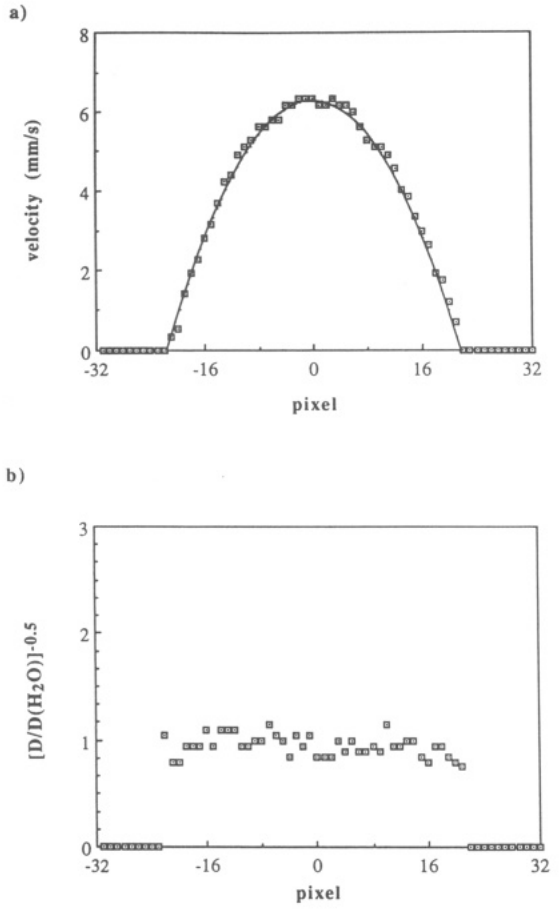

Figure 7. Profiles of the velocity and diffusion maps shown in Figure 6 for 0.5% w/v poly(ethylene oxide)/water solution in flow through a 700-μm-i.d. capillary. The water solvent diffusion coefficients are normalized to that of free water. The solid line in a corresponds to Poiseulle flow for which $n = 1$ in eq 10.

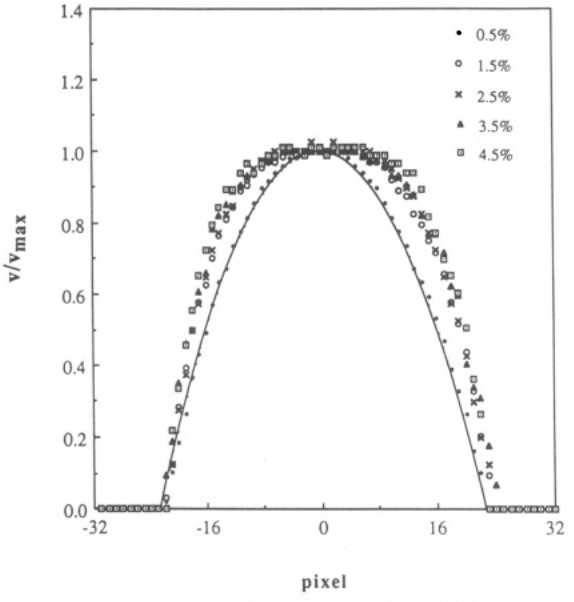

Figure 8. Normalized velocity profiles for different concentration solutions of poly(ethylene oxide) in water. A transition from Newtonian to shear-thinning behavior is apparent as the concentration is increased above c^*.

assumes a boundary condition with zero velocity at the capillary wall. This zero-slip condition is in fact consistent with the data presented here. We are able to locate the edge of the image with the resolution of one pixel. The velocity profiles concentrations of PEO/water used in this

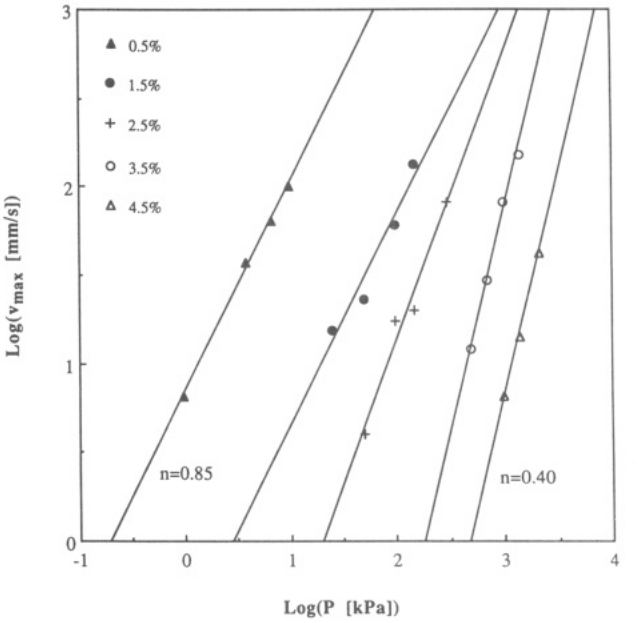

Figure 9. Double-logarithmic plot of v_{max} versus the pressure for different concentrations of poly(ethylene oxide)/water solutions. The data are well-described by the power law form of eq 11, with the exponent n varying from 0.85 for the lowest concentration to 0.40 for the highest.

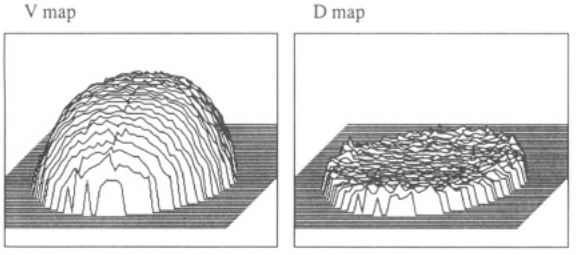

Figure 10. Velocity and self-diffusion maps for a 4.5% w/v poly(ethylene oxide)/water solution in flow through a 700-μm-i.d. capillary.

work for all extrapolate to zero within this resolution. We therefore find no evidence for slip.

The dependence of v_{max} on $(\Delta P/2K\Delta L)^{1/n}$ is tested in Figure 9. The data are clearly consistent with power law behavior but with an apparent exponent that decreases gradually with increasing concentration. For example, an exponent of 0.4 is suggested for the highest concentration used (4.5% w/v) while at lower concentrations the apparent exponent is closer to 1, the index for Newtonian flow.

The velocity and diffusion maps and corresponding profiles obtained at 4.5% concentration w/v and at a pressure head of 2100 kPa are shown in Figures 10 and 11. In this case v_{max} is 7.4 mm s^{-1}, and the maximum shear rate at $r = R$ is approximately 70 s^{-1}. Power law fits to the velocity profile exponents of 0.35, 0.40, and 0.45 are also shown. Again the 0.4 exponent works well. It is interesting that this same exponent has been found in laser Doppler anemometry experiments by Mackley[28] using polyethylene melts in capillary flow. It should be noted that we attach no particular significance to the power law constitutive equation and that other empirical models may describe the velocity profiles as well. In fact we observe that the central region of the measured velocity profile exhibits less shear than indicated by the power law fit. Such a feature is incorporated in the Bingham plastic description[2] in which the central region of such capillary flow is presumed to manifest pluglike behavior.

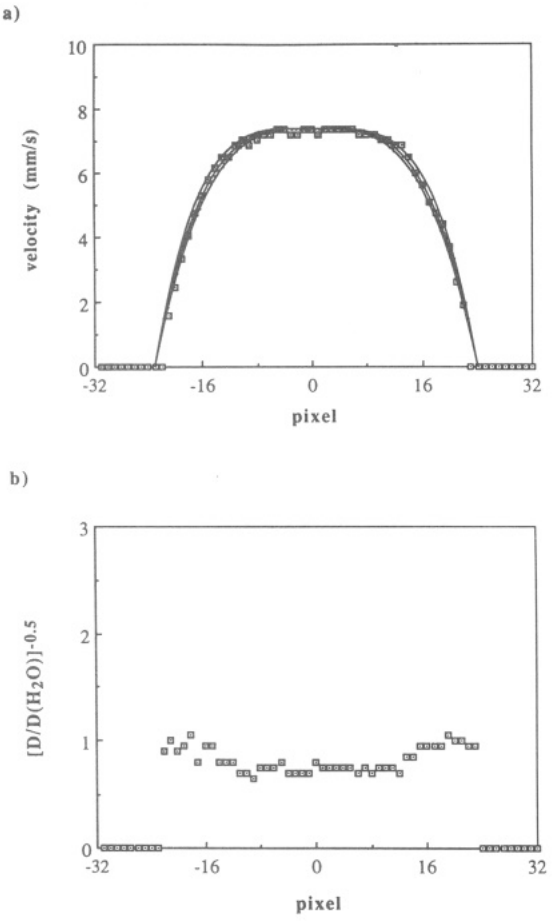

Figure 11. Profiles of the velocity and diffusion maps shown in Figure 10 for a 4.5% w/v poly(ethylene oxide)/water solution in flow through a 700-μm-i.d. capillary. The fits to the velocity profiles correspond to the power law fluid (eq 10) with exponents 0.35, 0.4, and 0.45. The best fit is given by $n = 0.4$, consistent with Figure 9. Note that the self-diffusion map refers to the predominant water molecules. Some enhancement is apparent in the shear-thinning region.

The existence of a critical radius in capillary flow is also consistent with the predictions of the Doi–Edwards model, which is based on a microscopic description of the polymer dynamics. We have not attempted to fit the velocity profiles using the Doi–Edwards theory because of the sensitivity of this model to molar mass and the high polydispersity of the polymer used in this work. It is clear, however, that the model can fit the data quite well. Nonetheless we shall appeal to the tube/reptation model in seeking to explain the local molecular dynamics exhibited via the shear dependence of the polymer self-diffusion coefficients, data which are more directly linked to the molecular depiction inherent in this theory.

The self-diffusion coefficients of the water and polymer molecules must be determined in separate experiments because of their significant difference in magnitude ($\sim 10^{-9}$ $m^2\ s^{-1}$ vs 10^{-14} $m^2\ s^{-1}$) and the need to suppress the signal from the solvent in the latter case. The water diffusion profile shown in Figure 11 does not exhibit the uniformity found for the 0.5% w/v PEO solution in capillary flow. In the 4.5% w/v solution under flow, enhanced water diffusion is apparent in the region of high shear near the capillary walls. The polymer self-diffusion profiles are measured by using the double PGSE imaging sequence shown in Figure 3b with reconstruction from a single projection. The quality of velocity compensation in these measurements is excellent as apparent in the comparative single and double PGSE velocity maps shown in Figure

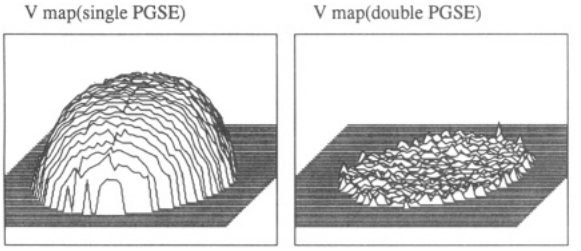

Figure 12. Comparison of the velocity maps obtained when single and double PGSE phase-encoding is employed. In the latter case the phase shifts due to velocity are cancelled and a null map is obtained.

12. Figure 13 compares polymer diffusion profiles for two adjacent chords in the vicinity of the capillary diameter. Figure 13a results from coadding the diffusion maps from 9 independent experiments while Figure 13b is obtained by coadding each of the 10 modulus images for corresponding g values and computing the diffusion map from the resulting set. These four maps are mutually self-consistent. Furthermore, in another experiment performed several months later using an independently prepared polymer solution, precisely the same diffusive behavior was observed. In each case the data exhibit a central region in which the self-diffusion coefficient is constant and less than or on the order of 10^{-13} $m^2\ s^{-1}$, but the diffusion coefficients rise sharply at a radius $\mathbf{r} \approx 0.5R$, increasing in an approximately linear manner with the radius until reaching a maximum value of around 5.5×10^{-13} $m^2\ s^{-1}$. The diffusion plateau in the capillary center is in fact quite consistent with the equilibrium D_s value of 10^{-14} $m^2\ s^{-1}$ for 4.5% w/v WSR301 PEO in water since the lower limit for diffusion measurement is approximately 10^{-13} $m^2\ s^{-1}$ in the imaging experiment given the available signal-to-noise ratio. It should also be noted that in the central region of the capillary the undisturbed tube renewal takes its longest value, τ_d. Because Δ is somewhat smaller than τ_d, this means that the center of mass diffusion is difficult to observe in this region.

One possible explanation for diffusive enhancement, as the shear rate increases, is the influence of self-diffusion transverse to the flow, since such motion in the presence of the velocity shear will cause a net phase shift in the double PGSE method. We have previously shown[15] that this effect leads to apparent diffusion enhancement by $1 + \dot{\gamma}^2\Delta^2 D_\perp/D_\parallel$. This factor could cause a doubling of the diffusion in the maximum shear region close to the walls ($r > 0.9R$), assuming that $D_\perp/D_\parallel$ is unity. However, there is reason to believe that $D_\perp/D_\parallel$ is less than unity! Further from the wall, the enhancement due to this transverse diffusion effect should be much smaller. It is most unlikely that this effect could cause the observed diffusive enhancement by nearly 2 orders of magnitude above the equilibrium D_s value.

Discussion

The enhancement of polymer self-diffusion above a critical shear rate provides dramatic evidence for the molecular basis of shear thinning. We picture this enhancement as arising from the breakdown of polymer entanglements as the shear rate exceeds the rate of tube renewal, τ_d^{-1}. The data provide three related but separate quantitative tests for any model. First, there is the value of the radius (and hence shear rate) at which enhancement occurs. Second, beyond this critical radius the dependence of the local polymer self-diffusion coefficient upon local shear rate may be used to provide confirmation of the theory. Finally, the existence of a plateau maximum value for the

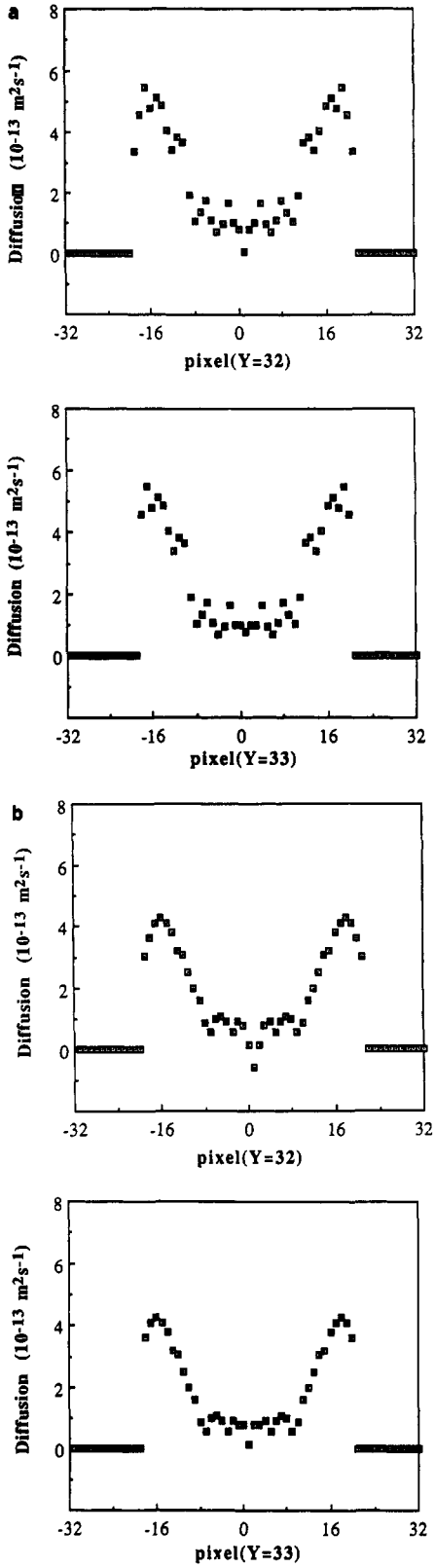

Figure 13. Polymer self-diffusion profiles for semidilute 4.5% WSR301 poly(ethylene oxide) (4.5% w/v in D_2O) under flow in the 700-μm-i.d. capillary under the same velocity shear indicated in Figure 11, but using a double PGSE (velocity nulling) imaging sequence. Dramatic enhancement is apparent beyond half the radius, consistent with the onset of shear-thinning when the shear rate exceeds the tube renewal rate, τ_d^{-1}. The data show profiles through two adjacent diametral chords across the capillary center by two different analyzing methods. Data in a show the result of averaging the diffusion maps from 9 independent experiments while the data in b show the diffusion map obtained when the independent "q-slice" maps are preaveraged before performing the Stejskal–Tanner analysis.

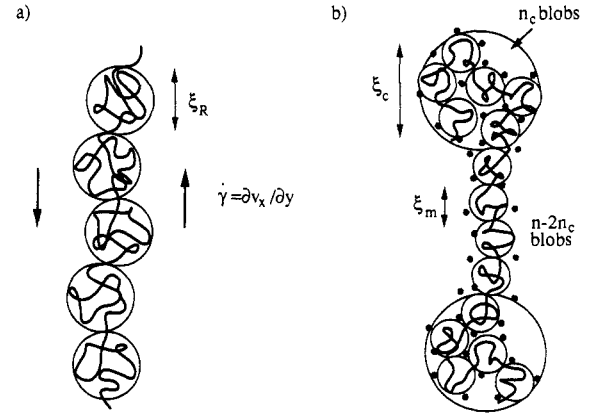

Figure 14. Schematic model of polymer stretching under velocity shear: (a) The Onuki model in which the dilute polymer coil elongates into a sequence of "Rouse blobs" each with relaxation rate equal to the local shear rate. (b) Depiction of coil deformation under shear for semidilute conditions. While the total tube length, L, and total tube renewal time, τ_d, are unaltered, only the ends of the coil can undergo tube renewal as fast as the local shear rate. The dimension ξ_c of the "end-blobs" (comprising n_c screening length blobs of dimension ξ_m) is therefore determined by $\dot{\gamma}$. The longitudinal self-diffusion of the polymer is enhanced due to the length extension.

polymer self-diffusion close to the capillary wall, along with the precise value of this maximum, provides yet another test.

By using the power law fit to the velocity profile, we may calculate the shear rate, which corresponds to the critical radius r_c, since

$$\frac{\partial v}{\partial r} = -\left(\frac{v_{max}}{R}\right)\left(\frac{n+1}{n}\right)\left(\frac{r}{R}\right)^{1/n} = -\left(\frac{\Delta P r}{2K\Delta L}\right)^{1/n} \quad (11)$$

hence, for $r_c = 0.5R$, $v_{max} = 7.4$ mm s^{-1}, and $R = 350$ μm, we find the critical shear rate to be (0.08 s)$^{-1}$. By comparison the tube renewal time may be calculated from our knowledge of the equilibrium self-diffusion coefficient since from the tube model

$$\tau_d = R_0^2/3\pi^2 D_s \quad (12)$$

where R_0 is the rms end-to-end length of the polymer. Using a value of $R_0 \approx 1500 \pm 300$ Å for 1.6×10^6 poly(ethylene oxide) in water, we find $\tau_d \approx 0.08 \pm 0.03$ s. τ_d^{-1} is sufficiently close to the observed critical shear rate to suggest that the tube model may provide a useful approach in understanding the basis of shear thinning.

Our depiction of the mechanism for diffusion enhancement is an adaptation of a proposal by Onuki[29] to explain coil stretch under simple shear for dilute polymer solutions. One normally associates coil stretch only with extensional flow. In Onuki's model the dilute coil forms a series of Rouse blobs of dimension ξ_R aligned along the direction of shear as shown in Figure 14a. While this extension is clearly unstable, the complete coil flips that occur from time to time are considered to be a rapid but occasional perturbation in the dilute-solution model. Each blob is characterized by a Rouse relaxation rate, τ_R^{-1}, equal to the shear rate $\dot{\gamma}$. This identity leads to the relation

$$k_B T/\xi_R^3 \eta_0 \approx \dot{\gamma} \quad (13)$$

where η_0 is the solvent viscosity. The identity can also be obtained by equating the force required to unravel one blob, $k_B T/\xi_R$, to the shear force acting on a neighboring blob displaced in the flow by one blob diameter,

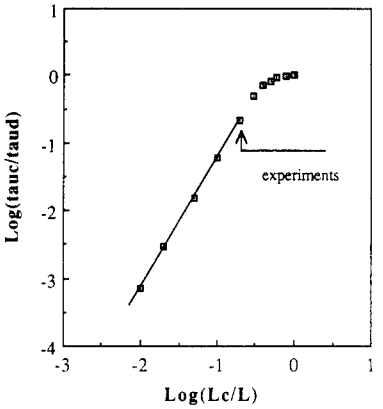

Figure 15. Relationship between the e^{-1} relaxation time, τ_c, and the length of the end tube, L_c, in the Doi–Edwards model. The arrow indicates the range of τ_c/τ_d corresponding to the shear rates apparent in the capillary flow experiment on the 4.5% w/v poly(ethylene oxide) solution.

$(6\pi\eta_0\xi_R)\dot{\gamma}\xi_R$. This equality forms the basis of the assumption that the polymer unravels into a sequence of aligned blobs.

The extension to semidilute solution is based on the depiction shown in Figure 14b. Suppose we focus our attention on one labeled chain. Because the tube is defined by surrounding chains that are in relative motion because of the shear, the tube topology is being continually redefined. For $\dot{\gamma} < \tau_d^{-1}$ the labeled chain re-forms its tube more rapidly than the shear rate so that the topology is unperturbed in relation to equilibrium. For $\dot{\gamma} > \tau_d^{-1}$ only the ends of the chain will be able to form a tube whose primitive path has the conformation of a random coil. The size of this end region, ξ_c, will be determined by the relaxation time τ_c for "end tube" renewal with $\tau_c^{-1} = \dot{\gamma}$. Between the end sections of dimension ξ_c, the chain will be extended in a linear sequence of blobs of dimension ξ_m, the concentration-dependent screening length. The end sections will consist of n_c such blobs arranged in the usual random path since only at the ends is the chain able to explore all possible conformations.

In essence, therefore, while the total tube length remains unchanged and the total tube renewal time is identical with the equilibrium value of τ_d, the extension of the chain increases along the direction of shear. The tensile force associated with this loss of chain entropy will be counterbalanced by the drag on the end sections. This drag is, however, hard to estimate because of the difficulty in assigning an effective local viscosity. An alternative approach to calculating n_c (and, hence, ξ_c) is to calculate τ_c from reptation theory. The probability $\varphi(s,t)$ that a segment s of the primitive path of total length L remains at a time t is given by[6]

$$\varphi(s,t) = \sum_{p\ \mathrm{odd}} \frac{4}{p\pi} \sin\left(\frac{p\pi s}{L}\right) \exp(-p^2 t/\tau_d) \qquad (14)$$

Integrating over a length L_c at the end of the chain gives an average probability

$$\varphi(t) = \sum_{p\ \mathrm{odd}} \frac{4L}{p^2\pi^2 L_c}\left(1 - \cos\left(\frac{p\pi L_c}{L}\right)\right) \exp(-p^2 t/\tau_d) \qquad (15)$$

$\varphi(t)$ is dominated by components for which p is a multiple of L/L_c. Hence, the longest relaxation time is on the order of $\tau_d(L_c/L)^2$.

Numerical examination of eq 15 shows that the e^{-1} relaxation time for $\varphi(t)$ depends quadratically on L_c/L only for $L_c < 0.2L$, as shown in Figure 15. For larger values the dependence is weaker. In the experiments carried out here the shear rate ranges from below τ_d^{-1} to approximately $5\tau_d^{-1}$ at the edge of the capillary, a regime that contains only a small "quadratic" region as indicated in Figure 15. The average dependence of τ_c/τ_d on L_c/L is approximately linear over this region. In applying the end tube model, we shall use both the linear approximation and a direct functional dependence of τ_c/τ_d on L_c/L obtained by fitting a fourth-order polynomial to the points shown in Figure 15. Thus, we may define a function f such that

$$L_c/L = f(\tau_c/\tau_d) \qquad (16)$$

In applying the condition $\dot{\gamma} = \tau_c^{-1}$, it is helpful to make use of the equilibrium relationships for a "melt of n blobs", where each blob of size ξ_m is governed by the usual dilute-solution statistics. Thus

$$\xi_m \approx b g^{\nu} \qquad (17)$$

$$\tau_d \approx 3\pi\eta_0 n^3 \xi_m^{\ 3}/k_B T \qquad (18)$$

where g is the number of statistical subunits of size b per blob. The total number of statistical subunits in the chain is given by $N = ng$. ξ_m and g are defined by the equilibrium concentration since $c \approx mg/\xi_m^3$ where m is the mass of one subunit. Since the concentration c^* may be defined in a manner similar to that of mN/R_0^3, useful empirical estimates for n and ξ_m are given by[6]

$$n = (c/c^*)^{1/(3\nu-1)} \qquad (19)$$

$$\xi_m = R_0(c/c^*)^{-\nu/(3\nu-1)} \qquad (20)$$

Since $L = n\xi_m$ and $L_c = n_c\xi_m$, application of the linear dependence assumption, $\tau_c = \tau_d(L_c/L)$, to eq 18 yields

$$n_c = [k_B T/3\pi\eta_0\dot{\gamma}\xi_m^{\ 3}n^2] \qquad (21a)$$

Alternatively, using the exact functional dependence, we find

$$n_c = nf(k_B T/3\pi\eta_0\dot{\gamma}\xi_m^{\ 3}n^3) \qquad (21b)$$

The self-diffusion coefficient for Brownian motion along the direction of shear may thus be estimated as

$$D_{\mathrm{shear}} \approx [2\xi_c + (n - 2n_c)\xi_m]^2/2\tau_d \qquad (22)$$

This equation will break down when the shear rate is less than or on the order of τ_d^{-1} since it does not account for the amalgamation of the two end tubes when $n \approx n_c$. However, it is clear that D_s approaches the equilibrium self-diffusion coefficient in this region so that we may directly assign this value when the shear rate is small. For large shears, such that $n_c \ll n$, the end tubes disappear and eq 22 predicts a maximum self-diffusion rate

$$D_{\mathrm{max}} = 3nD_s \qquad (23)$$

We may, therefore, speculate that the maximum diffusion rate apparent in the region near the capillary edge corresponds to a polymer in which the shear rate is sufficiently large that no end-tube entanglements are present. Given an apparent c^* of order 0.5% w/v and an equilibrium D_s value of 1×10^{-14} m^2 s^{-1}, D_{max} should be on the order of 5×10^{-13} m^2 s^{-1}. This is remarkably close to the observed value.

The model used here to explain the diffusive enhancement for $r > 0.5R$ is consistent with the notion that center-of-mass diffusion can be effectively observed, despite the fact that $\Delta < \tau_d$. In this enhancement region the linear

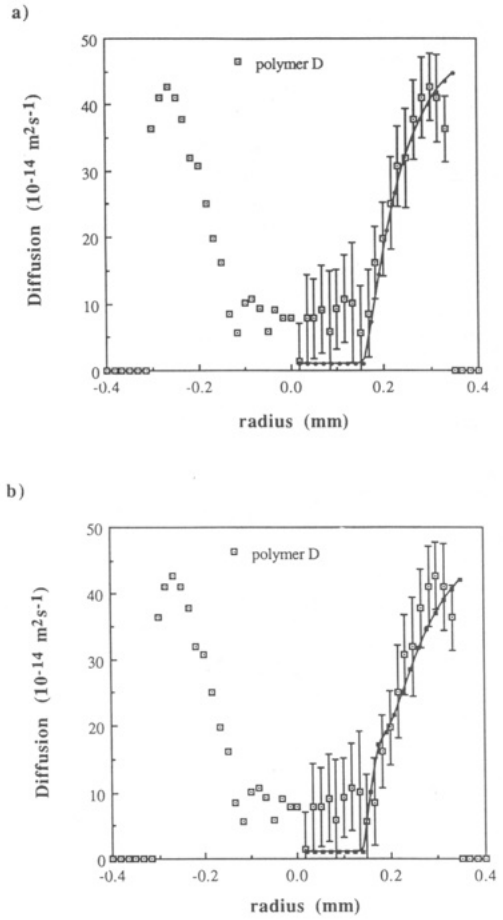

Figure 16. Experimental and theoretical polymer diffusion profiles for the 4.5% w/v poly(ethylene oxide) solutions in flow. The theoretical lines are based on the model depicted in Figure 14b, with (a) the linear approximation and (b) the exact functional dependence for the τ_c/τ_d vs L_c/L relationship shown in Figure 15. The only adjustable parameter is the polymer end-to-end distance, R_0, which is set at 1400 Å in a and 1300 Å in b.

extension of the central section of the polymer implies that semilocal internal motion and center-of-mass diffusion along the direction of flow are indistinguishable. Furthermore, curvilinear reptation, which results in differing laboratory-frame components of semilocal and center-of-mass motion, occurs only at the polymer ends and then with a relaxation time, τ_c, which is shorter than the observation time Δ.

Equations 19–22 enable the diffusion profile to be calculated directly from a knowledge of R_0 and c^* alone, without the need for any additional adjustable parameters apart from the power law exponent, ν, which for convenience we have assigned the value 0.6. Of course, our estimates of 1500 Å and 0.5% w/v, respectively, are somewhat coarse given the polydispersity of WSR301 PEO. Nonetheless they serve in providing a reasonable test of the model. The theoretical curve based on these parameters and using the approximate linear dependence of end-tube relaxation on L/L_c is shown in Figure 16a. The best fit to the data results R_0 = 1400 Å is used. Figure 16b shows the theoretical prediction when the end-tube relaxation rate has the correct functional dependence on L/L_c. In this case the best fit results when R_0 = 1300 Å. Both models reproduce several key features of the data. There is a sharp break in D_{shear} at a critical radius of about $^1/_2$ the radius of the capillary. The dependence of D_{shear} on the radius beyond the critical radius is approximately linear, and at high shear rates near the edge of the capillary,

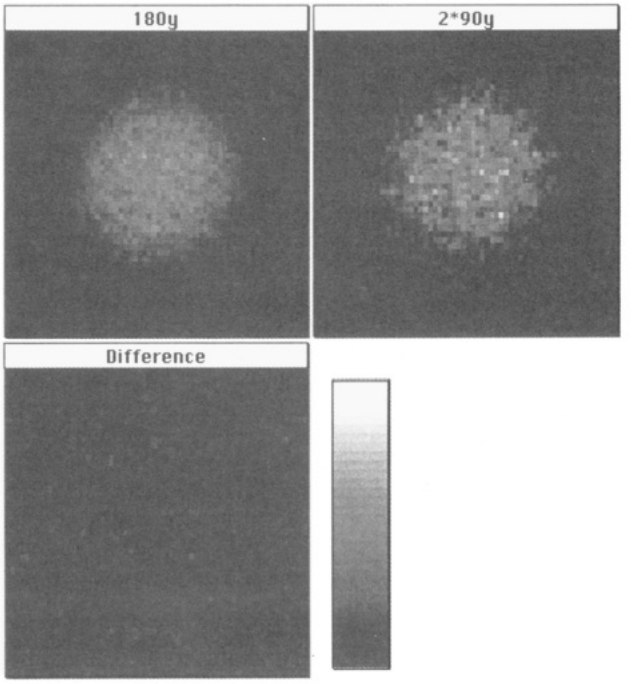

Figure 17. ^{1}H NMR spin-echo amplitude maps for semidilute WSR301 poly(ethylene oxide) (4.5% w/v in D_2O) under the flow conditions depicted in Figure 10. Both Hahn and solid-echo images are obtained, the latter being able to refocus decay due to anisotropic dipolar interactions. The images enable comparison of the relative amplitudes where shear thinning is occurring. The difference map (obtained on normalizing to the central image amplitudes) shows no additional refocusing in the solid echo, thus indicating the absence of polymer orientation at the local segmental level.

the theoretical values of D_{shear} rises less rapidly, approaching a plateau value of $3nD_s$. However, it is clear that this plateau is not quite reached in the theoretical prediction so that this feature of the data cannot be explained by using the simple model employed here.

The perturbation to polymer entanglement caused by the fluid shear will inevitably influence the Brownian motion of the solvent molecules, although this effect is bound to be quite minor in comparison with the polymer motion. The small enhancement of water diffusion apparent in Figure 11 is consistent with this effect. Finally we note that it is also possible to probe very local molecular properties using NMR relaxation times. In the present instance we have investigated whether there is evidence for local molecular ordering in the high shear region of the capillary. Any alignment will inevitably result in anisotropy of the proton–proton dipolar interaction in the CH_2 groups of the poly(ethylene oxide) segments. This would be manifested via enhanced transverse relaxation in a Hahn echo experiment although the dephasing caused by this local order would be refocused in a solid echo. Figure 17 shows comparative Hahn and solid echo polymer images obtained for the 4.5% w/v WSR301 poly(ethylene oxide)/D_2O solution under the same flow conditions that produced diffusion enhancement. After compensating for the lower signal efficiency of the solid echo (approximately a factor of 2), it is clear that there is no evidence for shear-dependent relaxation effects so that the measurement suggests orientational disorder on a local scale. This is entirely consistent with the depiction of Figure 14b where alignment occurs only on a scale larger than a blob.

Conclusion

Our analysis must necessarily be tempered by the fact that the polymer used in these capillary flow experiments

is highly polydisperse. Nonetheless, several conclusions may be drawn. Dynamic NMR microscopy may be used to provide precise velocity profiles to a spatial resolution of a few tens of microns, while at the same time making accessible measurements at the molecular level at various positions in the flow field. In particular, we have shown that it is possible to measure self-diffusion rates some 4 orders of magnitude slower than that of the free water molecule in a flow field where the velocity spread in a single pixel greatly exceeds the spread due to Brownian motion.

In the present work we see clear evidence for the breakdown of entanglements in semidilute solutions once the shear rate exceeds the equilibrium tube renewal rate, τ_d^{-1}, and we note that the method provides a nice, independent measurement of the tube renewal rate using NMR. Application of some simple ideas from reptation theory and the blob model for semidilute polymer solutions has proven remarkably successful in explaining several qualitative features of the data. A more precise analysis awaits a repeat of these experiments using monodisperse polymer.

Acknowledgment. We are grateful to Dr. R. K. Lambert of Massey University for valuable discussions and to Dr. Karl Amundson of Bell Laboratories for helpful criticism. The GPC analysis was carried out by Dr. R. Wang.

References and Notes

(1) Ferry, J. D. *Viscoelastic Properties of Polymers*, 3rd ed.; Wiley: New York, 1980.
(2) Skelland, A. H. P. *Non-Newtonian Flow and Heat Transfer*; John Wiley and Sons: New York, 1967.
(3) Doi, M.; Edwards, S. F. *J. Chem. Soc., Faraday Trans.* **1978**, *74*, 1789.
(4) Doi, M.; Edwards, S. F. *J. Chem. Soc., Faraday Trans.* **1978**, *74*, 1802.
(5) Doi, M.; Edwards, S. F. *J. Chem. Soc., Faraday Trans.* **1978**, *74*, 1818.
(6) Doi, M.; Edwards, S. F. *The Theory of Polymer Dynamics*; Oxford University Press: Oxford, 1987.
(7) Vinogradov, G. V. *Rheol. Acta* **1973**, *12*, 273.
(8) McLeish, T. C. B.; Ball, R. *J. Polym. Sci. Polym. Phys. Ed.* **1986**.
(9) Leger, L.; Hervet, H.; Rondelez, F. *Macromolecules* **1981**, *14*, 1732.
(10) de Gennes, P.-G. *J. Chem. Phys.* **1971**, *55*, 572.
(11) de Gennes, P.-G. *Scaling Concepts in Polymer Physics*; Cornell University Press: Ithaca, NY, 1979.
(12) Edwards, S. F. *Polymer* **1985**, *26*, 163.
(13) de Gennes, P.-G. *Macromolecules* **1976**, *9*, 587.
(14) Callaghan, P. T.; Eccles, C. D.; Xia, Y. *J. Phys. E: Sci. Instrum.* **1988**, *21*, 820.
(15) Callaghan, P. T.; Xia, Y. *J. Magn. Reson.* **1991**, *91*, 326.
(16) Mansfield, P.; Morris, P. G. *Advances in Magnetic Resonance, NMR Imaging in Biomedicine*; Waugh, J. S., Ed.; Academic Press: New York, 1982; suppl. 2.
(17) Stejskal, E. O.; Tanner, J. E. *J. Chem. Phys.* **1965**, *42*, 288.
(18) Callaghan, P. T. *Aus. J. Phys.* **1984**, *37*, 359.
(19) Callaghan, P. T.; Pinder, D. N. *Macromolecules* **1980**, *13*, 1085.
(20) Callaghan, P. T.; Pinder, D. N. *Macromolecules* **1981**, *14*, 1334.
(21) Callaghan, P. T; Pinder, D. N. *Macromolecules* **1984**, *17*, 431.
(22) Bachus, R.; Kimmich, R. *Polymer* **1983**, *24*, 964.
(23) Huirua, T. M.; Wang, R.; Callaghan, P. T. *Macromolecules* **1990**, *23*, 1989.
(24) Xia, Y. MSc Thesis, Massey University, 1988, unpublished.
(25) Callaghan, P. T.; Pinder, D. N. *Macromolecules* **1985**, *18*, 373.
(26) Callaghan, P. T.; Lelievre, J. *Anal. Chim. Acta* **1986**, *189*, 145.
(27) Bortel, E.; Kochanowski, A. *Makromol. Chem., Rapid Commun.* **1980**, *1*, 205.
(28) Mackley, M. R. *J. Non-Newtonian Fluid Mech.* **1986**, *21*, 337.
(29) Onuki, A. *J. Phys. Soc. (Jpn.)* **1985**, *54*, 3656.

Registry No. PEO, 25322-68-3.